# Robust probabilities of detection and quantification uncertainty for aerial methane detection: Examples for three airborne technologies

Bradley M. Conrad, David R. Tyner, Matthew R. Johnson [*]

*Energy & Emissions Research Laboratory, Department of Mechanical and Aerospace Engineering, Carleton University, Ottawa, ON K1S 5B6, Canada*

ABSTRACT

Thorough characterization of probabilities of detection (POD) and quantification uncertainties is fundamentally important to understand the place of aerial measurement technologies in alternative means of emission limitation (AMEL) or alternate fugitive emissions management programs (Alt-FEMP); monitoring, reporting, and verification (MRV) efforts; and surveys designed to support measurement-based emissions inventories and mitigation tracking. This paper presents a robust framework for deriving continuous probability of detection functions and quantification uncertainty models for example aerial measurement techniques based on controlled release data. Using extensive fully- and semi-blinded controlled release experiments to test Bridger Photonics Inc.'s Gas Mapping LiDAR (GML)™, as well as available semi- and non-blinded controlled release data for Kairos LeakSurveyor™ and NASA/JPL AVIRIS-NG technologies, robust POD functions are derived that enable calculation of detection probability for any given source rate, wind speed, and flight altitude. Uncertainty models are separately developed that independently address measurement bias, bias variability, and measurement precision, allowing for a distribution of the true source rate to be directly calculated from the source rate estimated by the technology. Derived results demonstrate the potential of all three technologies in methane detection and mitigation, and the developed methodology can be readily applied to characterize other techniques or update POD and uncertainty models following future controlled release experiments. Finally, the analyzed results also demonstrate the importance of using controlled release data from a range of sites and times to avoid underestimating measurement uncertainties.

## 1. Introduction

Methane is a potent yet short-lived greenhouse gas and rapid reductions in methane emissions from energy, waste, and agriculture sectors are an essential part of the pathway to limiting global temperature rise (Arias et al., 2021; CCAC, 2021; IPCC, 2018). However, successful mitigation of emissions is contingent on the ability to reliably detect potential emissions from both known and unknown sources. Moreover, development of trustworthy emission inventories and tracking progress toward mitigation targets requires accurate measurements within defined uncertainties. This challenge is central to emerging monitoring, reporting and verification (MRV) efforts (European Commission, 2021) and the associated verification role of the United Nations International Methane Emissions Observatory (IMEO).

In recent years, a range of potential detection and/or measurement technologies have been explored with promise to significantly reduce time and labour costs to find and measure sources of methane, especially

for applications in the oil and gas sector (Bell et al., 2020; Fox et al., 2019; Kemp and Ravikumar, 2021; Rashid et al., 2020; Ravikumar et al., 2019; Schwietzke et al., 2019). Of particular interest are airplane-mounted technologies, which are increasingly used in large-scale field campaigns with success (Chen et al., 2022; Cusworth et al., 2021; Johnson et al., 2023; Tyner and Johnson, 2021) and gaining acceptance in alternate fugitive emissions management programs (Alt-FEMP) replacing or supplementing optical gas imaging (OGI) surveys using hand-held infrared cameras (EMNRD, 2023; AER, 2021; Bridger Photonics, 2021). With sensitivities >100–1000 times better than current satellite systems, airplane-mounted sensors have emerged as a key tool for mitigating methane, well-suited to the challenging "verification" component of MRV and capable of being used to create measurement-based inventories. However, successful application of these technologies and interpretation of collected data requires a thorough understanding of the probability of detecting unknown sources under different conditions and uncertainty in quantifying emissions

---

from detected sources. To date, only limited controlled release studies have appeared in the literature (Bell et al., 2020; Johnson et al., 2021; Ravikumar et al., 2019; Sherwin et al., 2021; Thorpe et al., 2016 plus (Bell et al., 2022) which appeared after final revisions of the present article prior to final publication) and robust methodologies to meet these requirements have not been developed.

This paper has four main objectives. First, a novel generalized approach to deriving continuous probability of detection (POD) functions is presented that significantly improves upon existing formulations in the literature that are often non-physical. Generalized POD functions are essential for understanding what is or is not captured in field measurements and modelling the applicability and mitigation potential of technologies in programs like FEAST (Fugitive Emissions Abatement Simulation Toolkit; Kemp et al., 2016). Second, a statistical error model is presented to derive quantification uncertainties in aerial-estimated source rates. Together with robust POD data, quantification uncertainties are essential for defensibly applying airborne measurements for MRV and ultimately for using aerial data in measurement-based inventories. Third, using extensive controlled release experiments completed to evaluate Bridger photonics' gas mapping LiDAR (GML)™ system (Bridger Photonics, 2021) as an initial case study, a continuous POD function and separate quantification uncertainty model are derived. Finally, using available published controlled release data, the methods are extended to also estimate robust POD and quantification uncertainty of Kairos LeakSurveyor™ (Kairos Aerospace, 2022) and POD of NASA's Jet Propulsion Laboratory's Next-Generation Airborne Visible/Infrared Imaging Spectrometer (AVIRIS-NG) platform (Thorpe et al., 2016).

## 2. Methodology

### 2.1. Methane detection technologies

#### 2.1.1. Bridger photonics gas mapping LiDAR™

Bridger Photonics Gas Mapping LiDAR (GML) uses an airplane-mounted scanning laser, camera, and Global Navigation Satellite System – Inertial Navigation System to detect methane sources and produce quantitative geo-located imagery of associated plumes (Bridger Photonics, 2021; Hunter and Thorpe, 2017; Johnson et al., 2021; Kreitinger and Thorpe, 2018). Originally developed through the Advanced Research Project Agency – Energy (ARPA-E) MONITOR program (ARPA-E, 2018), the technology uses wavelength modulation spectroscopy at 1651 nm to measure path-integrated methane concentrations between the aircraft and the ground, which acts as a topographic backscatterer. Forward and backward looking measurements as the plane flies give information on the detected plume height, typically within 2 m accuracy (Johnson et al., 2021). At typical target altitudes between 168 and 230 m above ground level (AGL), the sensor's 31° field-of-view results in an approximately 94–130 m wide measurement swath on the ground and resolves plumes with ~1–2 m spatial resolution. Source emission rates are estimated by a proprietary method that combines information about the spatial concentration of methane in the detected plume, the height of the plume above ground level, the horizontal wind speed at the time of detection (Bridger Photonics typically uses interpolated hourly meteorological station data from the public High-Resolution Rapid Refresh (HRRR) database (NOAA, 2020) or Meteoblue (http://meteoblue.com) depending on coverage in the region of interest), and the assumed vertical profile of wind speed. Preliminary analysis of blinded controlled releases by Johnson et al. (2021) suggests that 1σ quantification uncertainties of ±31–68% can be expected from a single pass of sources near the sensitivity limit. However, uncertainties at higher release rates and over a broader range of conditions are not well-described in the literature and a robust understanding of these uncertainties is an important goal of this paper.

#### 2.1.2. Kairos Aerospace LeakSurveyor™

Kairos Aerospace's LeakSurveyor is an airplane-mounted methane imaging system that combines an infrared imaging spectrometer, global positioning system (GPS) and inertial monitoring unit, and optical camera to detect methane plumes (Berman et al., 2021; Branson et al., 2021; Schwietzke et al., 2019). Path-integrated methane concentrations are measured via absorption of reflected sunlight from the ground in spectral regions where there is no interference from other common hydrocarbons (Berman et al., 2021). For the targeted flight altitude of 900 m AGL, each measurement swath is approximately 800 m wide with a spatial resolution of ~3 m (Sherwin et al., 2021). As summarized in Berman et al. (2021) and Sherwin et al. (2021), quantification is via a proprietary algorithm that calculates pixel-level methane column density between the airplane and the ground, sums these estimates within a core-plume region with distinguishable methane enhancements from background, divides by the length of this core plume region, and multiplies by an estimated wind speed. Compared to Bridger Photonics' *active* GML sensor, the *passive* LeakSurveyor from Kairos Aerospace trades potential advantages of larger measurement swath permitting greater facility coverage per airplane pass with the disadvantages of lower spatial resolution and higher minimum detection limits as well as potentially greater sensitivity to environmental lighting conditions.

Because in-situ wind speed is not generally available for aircraft-detected sources and database wind speed can be highly uncertain, Kairos Aerospace typically provides source rate estimates on a wind-normalized basis – i.e., in units of emission rate per wind speed (Branson et al., 2021). Kairos' in-house (Berman et al., 2021) and third-party (Sherwin et al., 2021) assessments of the LeakSurveyor technology have estimated detection sensitivities in these units of approximately 8.2 (at a 50% POD) and 5–15 (kg/h)/(m/s) ("partial detection range"), respectively. Quantification bias was also assessed by Kairos Aerospace on a wind-normalized source rate-basis and found to be approximately −2% (Branson et al., 2021); precision errors were not analyzed. In their controlled release study, Sherwin et al. (2021) independently evaluated quantification error in emission rate (non-normalized units of kg/h) by multiplying LeakSurveyor-reported wind-normalized source rate data by wind speed estimated from four different sources. The parity slope of estimated-to-controlled source rates ranged from 0.88 to 1.45×, representing a bias on the order of −12 to +45% depending on the source of wind speed data. Precision errors were estimated using the residuals of linear fits to controlled release data and were on the order of 30–42% (1σ).

#### 2.1.3. NASA JPL's next-generation airborne visible/infrared imaging spectrometer

The next-generation airborne visible/infrared imaging spectrometer (AVIRIS-NG; Hamlin et al., 2011) is an improvement on the original AVIRIS instrument (Green et al., 1998) developed by the U.S. National Aeronautics and Space Administration's (NASA) Jet Propulsion Laboratory (JPL). The AVIRIS-NG instrument is a push-broom imaging spectrometer with approximately 5 nm spectral resolution over the visible and near-infrared spectra (380 to 2510 nm). Methane point source detection studies have flown the AVIRIS-NG instrument at different altitudes: 430 to 3800 m AGL (Thorpe et al., 2016) and, more recently, 3000 to 8000 m AGL (Thorpe et al., 2021). For the approximately 34° field-of-view, swath widths and spatial resolutions are on the order of 1800 m and 3 m at a typical/common flight altitude of 3000 m AGL (Duren et al., 2019; Thorpe et al., 2021) and approximately 3300 m and 8 m at a flight altitude of 8000 m AGL. Methane columns are retrievable using differential optical absorption spectroscopy (e.g., Cusworth et al., 2019; Thorpe et al., 2017) or matched filter methods (e.g., Foote et al., 2020; Thompson et al., 2015) permitting downstream processing to identify methane plumes.

Although the development of AVIRIS(-NG) was not specifically motivated by methane detection, AVIRIS-NG has been successfully used to detect, map, and monitor large-scale methane emitters. Methane-

relevant studies have targeted measurements at an array of assorted facility types (Duren et al., 2019; Guha et al., 2020) with some focusing on oil and gas facilities (Cusworth et al., 2021; Frankenberg et al., 2016; Thorpe et al., 2020) solid waste facilities (Cusworth et al., 2020; Krautwurst et al., 2017), and arctic permafrost (Elder et al., 2020). In 2013, Thorpe et al. (2016) mounted the AVIRIS-NG instrument on a Twin Otter aircraft during controlled release experiments to evaluate methane retrieval algorithms and assess detection sensitivity as a function of wind speed and aircraft altitude. At the time of writing, the accuracy of methane source rate estimation using AVIRIS-NG has not been evaluated in detail, although a recent study focusing on the evaluation of an airborne Doppler wind LiDAR instrument (Thorpe et al., 2021) includes source quantification data for a pair of controlled release tests.

## 2.2. Controlled releases – Bridger GML

For this study, controlled methane releases were completed as part of two separate field campaigns during September 5–8, 2020 and August 19–22, 2021 at oil production sites near Lloydminster, Saskatchewan to assess Bridger Photonics' GML technology. These releases were completed as part of broader measurement surveys across western Canada and included both semi-blinded and fully blinded experiments to assess quantification accuracy as well as detection sensitivity under varying conditions. First, working collaboratively with Bridger Photonics and the contracted airplane operator, high-flowrate controlled releases were completed to derive GML quantification uncertainties when measuring methane sources emitting between 1 and 66 kg/h, consistent with 96% of sources found in a recent survey of oil and gas infrastructure in BC, Canada (Tyner and Johnson, 2021). These *semi-blinded* releases, where Bridger was told that controlled releases were being performed but not informed of the exact release locations within the facilities nor the flow rates, were made from a set of four inactive oil and gas facilities conveniently arranged in a line approximately 375 m apart (refer to supplemental information (SI) for additional detail). Over four days during each campaign, the plane flew laps over the test facilities while flow rates at each site were independently varied between each lap at predetermined random flow rates (including zero releases) that were not shared with Bridger Photonics nor the aircraft operator.

Second, following the same approach used in Johnson et al. (2021), additional low-flowrate controlled releases (0.4–5.2 kg/h) plus zero-releases were performed from active sites included in parallel contracted surveys of oil and gas infrastructure in the region. In collaboration with industry operators, methane was released from within facility premises at random rates near the expected sensitivity limit of the GML technology to test its ability to correctly detect unknown sources at unknown locations. These tests, performed considering impacts from interaction of the temporally varying wind with adjacent infrastructure and in the potential presence of additional sources from the active facilities, were fully blinded in that they were conducted without informing Bridger Photonics nor the aircraft operator that the experiments were taking place. Bridger provided final source detection

and quantification data (obtained using their internal analysis of Meteoblue wind data) without having access to data from the semi-blinded releases and without having been informed of the fully blinded release experiments.

At each release location time-resolved wind speed at 3 m above ground level was measured at 1 Hz using an ultrasonic wind sensor (Anemoment, TriSonica mini) with a rated accuracy of $\pm 0.2$ m/s over the relevant range of 0–10 m/s. Methane from compressed cylinders (PraxAir, >99% purity) was released through Bronkhorst thermal mass flow controllers (various models, rated accuracy of $\pm 0.1\%$ of full scale or $\pm 0.5\%$ of reading). For the larger flow rates, a custom-built heated regulator and liquid-gas heat exchanger system were used to overcome Joule-Thomson cooling of the gas and ensure temperatures were near ambient as it entered the flow controllers. The methane then flowed through at least ~20 m of tubing to a release point from a vertically oriented, 1 m length pipe (i.e., typical working height for oil and gas infrastructure) temporarily secured to the ground. GPS-synchronized data loggers were used to record methane release rate and wind speed data that could subsequently be matched with time-stamped data provided by Bridger. This was especially important in confirming missed detections during the fully blinded releases from within sites included in the parallel surveys of oil and gas infrastructure. Although exit temperature of each methane release was not measured, calculations confirm that the length of tubing was such that it would have been ambient in all cases, consistent also with the field experiments of Sherwin et al. (2021). Table 1 summarizes the controlled release experiments.

## 2.3. Available controlled release data for Kairos' LeakSurveyor

Using the new methodology presented below, a robust POD function and uncertainty model were also developed for Kairos' LeakSurveyor using published controlled release data from Sherwin et al. (2021) augmented with internal controlled release data obtained from Kairos as in Chen et al. (2022). Sherwin et al. (2021) completed 234 semi-blinded controlled release tests of Kairos' LeakSurveyor from a single facility located in San Joaquin County, California over four days spanning October 8–15, 2019. These included 210 non-zero controlled releases between 18 and 1025 kg/h. Three data points were discarded following Sherwin et al.'s (2021) initial quality control and the remaining 207 releases were used to assess detection sensitivity in the present work – 40 of these 207 releases were purposely performed at low flowrates near the lower limit of the flowmeter (<50 kg/h). Of the original 210 releases, 148 were considered for the present assessment of quantification error, corresponding to the subset of release data with a successful detection, a controlled rate > 50 kg/h, and no quality control concerns. Wind speeds were measured in situ at 8 ft. (~2.43 m) above ground level using two instruments: a cup-based wind meter and a two-dimensional ultrasonic anemometer (on the latter three days only). Sherwin et al. (2021)'s analysis also evaluated quantification error for the practical scenario where in-situ wind speed data are not available, testing

**Table 1**
Summary of controlled release experiments to test Bridger Photonics' GML completed as part of the present study.

| Release Set | Period | Count |
|---|---|---|
| High-flowrate (1–66 kg/h), semi-blinded releases from a fixed set of inactive facilities[a] | Sept. 5–8, 2020 | 138 (122 non-zero) |
| | Aug. 19–22, 2021 | 175 (162 non-zero) |
| Low-flowrate (0.4–5.2 kg/h), fully blinded releases from within active sites included in parallel oil & gas sector surveys[b] | Sept. 5–7, 2020 | 67 (38 Misses) |
| | Aug. 19–21, 2021 | 115 (24 Misses) |
| Total | 495 total releases | |

[a] All non-zero semi-blinded releases were detected.
[b] Representative scene noise was provided with the standard data product for small-volume releases in 2020 and 2021.

accuracy when using minute-resolved data from the commercial Dark Sky database (Apple Inc., 2022) and hourly data from the HRRR database (NOAA, 2020). The LeakSurveyor sensor was used to detect and, where possible, quantify the controlled releases and was flown at a nominal altitude of 900 m AGL throughout the study. For the present analysis of POD, in-situ wind speed from the ultrasonic anemometer is favoured when available due to its improved accuracy over the cup-based meter; for the measurement day where only data from the cup-meter were available, these data are corrected based on a linear fit with available ultrasonic data. Sherwin et al. (2021) chose the one-minute gust as the representative measured wind speed (corresponding to the maximum speed during the minute prior to the aircraft overpass) in the main text of their analysis, which matches the wind speed preferred in Kairos' quantification as further discussed below. By contrast, the present analysis uses the one-minute *averaged* wind speed prior to the aircraft overpass as it is likely to be more indicative of convective dispersion of the plume prior to detection and is the relevant windspeed to consider when planning a survey or modelling expected performance in simulators like FEAST. To standardize wind speeds against the present controlled releases, all available wind data were scaled to a 3-m height AGL using a logarithmic profile with a specified zero-displacement plane, $d$, of 0.066 m and a surface roughness, $z_0$, of 0.01 m representative of the graded areas around oil and gas areas as used in Bridger's algorithm (Johnson et al., 2021).

As in Chen et al. (2022), additional data from internal controlled release studies were provided by Kairos to augment the present analysis of detection probabilities and quantification error/uncertainty. These confidential data include controlled source rate, estimated wind-normalized source rate, measured wind speed, and one-minute gust wind speed from the Dark Sky database for 375 additional non-zero releases. Noting that the blindedness of Kairos' internal studies could not be evaluated, within these data a total of 45 releases were missed and 296 releases were automatically detected by Kairos' algorithm; the remaining 34 were tagged as partial detects, which required human interpretation to identify a plume. When combined with the publicly available controlled release data of Sherwin et al. (2021) (which are treated as automated detects since the available data did not distinguish partial detects), there were a total of 485 detects, 34 partial detects, and 63 missed detections. Additional analysis in the SI shows the effects of treating these data sets separately. For the quantification uncertainty modelling, where only sources >50 kg/h were considered and partial detections were not quantified, there were 148–376 available source measurements depending on which wind data source was considered.

### 2.4. Published controlled release data for NASA JPL's AVIRIS-NG

A POD function for the AVIRIS-NG sensor was derived using the controlled release data reported by Thorpe et al. (2016). These experiments were originally designed to evaluate the ability of AVIRIS-NG in detecting methane point sources and the available data do not include separate source rate estimates from the plane. A total of 143 non-blinded controlled releases were completed over seven days in June 2013 from three separate sites within the Rocky Mountain Oilfield Testing Center in Wyoming, U.S.A. Thorpe et al. (2016) measured wind speeds at 8–9 m AGL using a 3D ultrasonic wind anemometer. For the present analysis of detection probability, reported wind speeds (averaged over the minute preceding a detection) were scaled from an average height of 8.5 m AGL to 3 m AGL using the same logarithmic profile and parameters noted above; the resulting wind speeds at 3 m spanned 0.66–7.5 m/s. Controlled release rates ranged from 2.2 to 96 kg/h and flight altitudes were between 430 and 3800 m AGL. For each release, the methane plume was flagged as either detected (automatic detection by algorithm, $N = 94$), partially detected (requiring human interpretation, $N = 25$), or missed ($N = 24$).

## 3. Statistical analysis

### 3.1. Generalized approach to deriving robust probability of detection functions

For a specified remote detection technology, the probability of detection (POD) function represents the likelihood of successfully detecting an emitter at some source rate for a given set of conditions during a single measurement observation. Although different technologies may be affected by additional parameters, in general, detectability of a given source (at rate $Q$) depends on the wind field that drives plume dispersion, the spatial resolution of the measurement, and the effective signal-to-noise ratio (SNR) of the measurement system. For simplicity, the effects of wind can be parameterized by the true/measured 3-m wind speed ($u_3$). For Bridger's GML technology, the measured 3-m wind speed is computed from in-situ wind measurements at 1 Hz using Bridger's Gaussian smoothing algorithm. For the imaging spectrometers, measured wind speed is averaged over one minute prior to the aircraft overpass to be consistent with Sherwin et al. (2021). For a fixed set of sensor optics, the ground-level spatial resolution is defined by the altitude of the measurement system above ground level ($\widetilde{h}$ [m]). The effective SNR for a given measurement is itself a function of $Q$ and $u_3$ (which affect the observed path-integrated concentration of the plume), $\widetilde{h}$ (which affects signal strength through the inverse square law), the spectral albedo of the ground (which affects the strength of the return signal), and potentially other parameters specific to the technology. Although additional SNR data may or may not be readily available for a given technology as further considered below, it is initially considered in this general analysis as a representative scene noise in units of column density ($\widetilde{n}$ [ppm-m]). Using these parameters, a POD function can be derived that depends on $\boldsymbol{x} = \left[Q, u_3, \widetilde{h}, \widetilde{n}\right]^T$. Technically, the plume height ($\widetilde{z}_p$) is also a relevant parameter since plume dispersion is height-dependent; however, since this is undefined for a failed detection, it is necessarily ignored in the derivation of a POD function.

A broad range of potential POD functions were evaluated using binary regression on the collected controlled release data. The objective of binary regression is to model a binary dependent variable, here $D$ representing a successful (1) or failed (0, "missed") detection, which follows a Bernoulli distribution having the POD function, $POD(\boldsymbol{x})$, as its parameter, i.e.,

$$D \sim Bernoulli(\text{POD}(\boldsymbol{x})) \tag{1}$$

The POD function ($POD(\boldsymbol{x})$) is modelled as a composite of a "predictor" function ($g(\boldsymbol{x};\boldsymbol{\phi})$), with variables $\boldsymbol{x}$ and coefficients $\boldsymbol{\phi}$, and a *continuous* "inverse link" function ($F(g(\boldsymbol{x};\boldsymbol{\phi});\boldsymbol{\theta})$), with coefficients $\boldsymbol{\theta}$:

$$\text{POD}(\boldsymbol{x}) \equiv F(g(\boldsymbol{x};\boldsymbol{\phi}),\boldsymbol{\theta}) \tag{2}$$

For a candidate pair of predictor and inverse link functions, $\boldsymbol{\phi}$ and $\boldsymbol{\theta}$ are obtained by maximum likelihood estimation (MLE) of the Bernoulli distribution using controlled release data. This can be found via optimization to minimize $\ell$, the negative logarithm of the likelihood function, where for the Bernoulli distribution:

$$\ell(\boldsymbol{\phi},\boldsymbol{\theta}) = \sum_i -\left(D_i ln F_i + (1-D_i) ln(1-F_i)\right) \tag{3}$$

and $F_i = F(g(\boldsymbol{x}_i;\boldsymbol{\phi}),\boldsymbol{\theta})$ for each controlled release data point, $i$.

For a fixed probability of detection ($p$), the POD function may be inverted to define contours of constant sensitivity for the measurement technique. In the present case, this permits calculation of a critical source rate at some detection probability, as a function of the remaining parameters in $\boldsymbol{x}$ – i.e., $Q_p\left(u_3, \widetilde{h}, \widetilde{n}; p\right)$. A linear prediction model is often used in binary regression, such that $g(\boldsymbol{x}) = \boldsymbol{\phi}^T \boldsymbol{x}$, which is coupled with a logistic inverse link function (logistic regression) or a normal cumulative

distribution function (CDF; probit model). However, in the present application, this approach produces lines of constant detection probability that converge to zero at zero wind ($u_3 = Q_p = 0$) for a fixed aircraft altitude and scene noise. This implies that an infinitesimally small emitter could be detected as wind reduces toward zero, which is non-physical for a noise-laden system. To avoid this, candidate predictor functions are permitted to be nonlinear, while remaining monotonic with each element in $\boldsymbol{x}$ and non-negative (consistent with the definition of each element). Candidate predictor functions are also required to provide a non-negative output that increases with the likelihood of detection. The inverse link function then maps the output of the predictor function to a continuous POD between 0 and 1, as required.

### 3.2. Source quantification uncertainty

To interpret estimated source rate data, it is critical that measurement uncertainties are thoroughly understood. This section presents the method by which controlled release data can be used to derive predictive estimates for the true source rate ($Q$) given an estimated source rate ($\widetilde{Q}$). Mathematically, the objective is to derive the conditional probability of $Q$ given $\widetilde{Q}$ – i.e., $\pi\left(Q|\widetilde{Q}\right)$. This challenge was approached by parsing observed errors during controlled release experiments into bias and precision components.

Consider hypothetical multiple detections/measurements of a single, steady-state source observed on a single, specific date. It can be assumed that, *on average*, there will be some error in the estimated value of the source rate, which represents *bias* in the measurement of this source on the specific date. A bias-correction procedure that accounts for this average error in $\widetilde{Q}$ can be developed using a *bias-corrected* estimate of the source rate $\left(\widehat{Q} = f_B\left(\widetilde{Q}\right)\right)$, which may be assumed to follow a conditional distribution $\pi\left(\widehat{Q}|\widetilde{Q}\right)$. A *precision distribution* that accounts for precision error of the bias-corrected estimate can be similarly defined, $\pi(Q|\widehat{Q})$. The desired distribution of the true source rate given the estimated source rate can then be computed from these distributions via:

$$\pi\left(Q|\widetilde{Q}\right) = \int_{\widehat{Q}} \pi(Q|\widehat{Q})\, \pi\left(\widehat{Q}|\widetilde{Q}\right) d\widehat{Q} \tag{4}$$

where the integration is performed over all possible values of $\widehat{Q}$. For convenience, Eq. (4) can be re-written in terms of *probabilistic* correction parameters $\kappa_Q$ and $\lambda_Q$ – where $\kappa_Q = \widehat{Q}/f_B\left(\widetilde{Q}\right)$ is a bias-correction parameter and $\lambda_Q = Q/\widehat{Q}$ is a precision-correction parameter – that are *statistically independent* from $\widetilde{Q}$, $\widehat{Q}$, and $Q$. Letting the probability distributions of these correction parameters be $\pi_{\kappa_Q}(\kappa_Q)$ and $\pi_{\lambda_Q}(\lambda_Q)$, respectively, their statistical independence implies via a change of variables that $\pi(Q|\widehat{Q}) \equiv \pi_{\lambda_Q}(Q/\widehat{Q})/\widehat{Q}$ and $\pi\left(\widehat{Q}|\widetilde{Q}\right) \equiv \pi_{\kappa_Q}\left(\widehat{Q}/f_B\left(\widetilde{Q}\right)\right)/f_B\left(\widetilde{Q}\right)$. Introducing these into Eq. (4) gives:

$$\pi\left(Q|\widetilde{Q}\right) = \int_{\widehat{Q}} \pi_{\lambda_Q}\left(\frac{Q}{\widehat{Q}}\right) \pi_{\kappa_Q}\left(\frac{\widehat{Q}}{f_B\left(\widetilde{Q}\right)}\right) \frac{1}{\widehat{Q} f_B\left(\widetilde{Q}\right)} d\widehat{Q} \tag{5}$$

Since bias-correction accounts for the average error in $\widetilde{Q}$, the parameters of the precision-correction distribution ($\pi_{\lambda_Q}$) must be chosen to yield a unit mean. Likewise, the parameters of the bias-correction distribution ($\pi_{\kappa_Q}$) can be constrained to have a unit mean to permit consideration of measurement bias through the optimized coefficient(s) of the bias-correction function ($f_B$).

There is one simplifying limiting case for the conditional distribution shown in Eq. (5) that is necessary if controlled release data are constrained to a small set of sites and/or measurement days. In this case, measurement error must be assumed to be *independent* of time and

location, implying that the required bias-correction is non-probabilistic. With this assumption, Eq. (4) simplifies to:

$$\pi\left(Q|\widetilde{Q}\right) = \pi_{\lambda_Q}\left(\frac{Q}{f_B\left(\widetilde{Q}\right)}\right) \frac{1}{f_B\left(\widetilde{Q}\right)} \tag{6}$$

The conditional probability distributions in Eq. (6) were computed via MLE using controlled release data for Bridger's GML and Kairos' Leak-Surveyor technology. This approach optimizes the parameters for $\pi_{\lambda_Q}$ (constrained to yield a unit mean) and the coefficients of the bias-correction function, $f_B$.

Myriad other parameters could influence error in source rates estimated from aerial measurements. These include the time-history of the turbulent wind field over the site as well as parameters impacting the quality of the measurement signal (e.g., aircraft altitude/orientation and surface albedo). In the most general sense, the desired probability distribution(s) should be conditioned on these additional parameters. However, error caused by these parameters are likely to be highly site-, source-, and time-dependent, such that these confounding variables are inherently considered if extensive controlled release data for multiple sites over multiple days are available and Eq. (5) can be used to model quantification error. Conversely, since Eq. (6) assumes errors are independent of site, source, and time, this latter model can be expected to underestimate variance in the quantification error. Sufficient data were obtained during the high-flowrate controlled release experiments of Bridger's GML to permit evaluation of quantification error via both Eq. (5) and (6). This case study identifies the importance of site- and day-dependent quantification error as discussed in Section 4.2.1 below.

## 4. Results

### 4.1. Probability of detection

Starting first with the detailed case-study of Bridger's GML, Fig. 1a plots the 466 non-zero controlled releases obtained during the 2020 and 2021 campaigns as a function of measured 3-m wind speed, calculated from in-situ measurements following Bridger's Gaussian smoothing algorithm. Successful detections of fully and semi-blinded releases are identified in blue and green, respectively, and misses in red. There were no false positives during the 29 zero controlled releases. Over this range of wind speeds between 0.5 and 7.2 m/s, all controlled release sources greater than ~4.5 kg/h were detected. Fig. 1b shows a magnified view of the same data for source rates <8 kg/h, which highlights the probabilistic nature of detection success.

Expectedly, successful detection appears more likely at higher source rates and lower wind speeds – i.e., detection probability is correlated with the wind-normalized source rate as in previous studies (e.g., Sherwin et al., 2021). This is anticipated by the simplified Gaussian plume dispersion model (Hanna et al., 1982), where the wind-normalized source rate is proportional to the plume column density along the vertical axis (i.e., the observable "signal" for an airborne measurement). However, detection is also affected by the strength of the return signal at the optics which is proportional to $\widetilde{h}^{-2}$ (inverse square law) and the spatial resolution of the imagery, which for Bridger's scanning laser and GML optics is approximately proportional to $\widetilde{h}^{-0.5}$. Including these effects, while still ignoring the effect of instrument noise for the time-being, provides an informative, non-parametric, *simple* predictor function for Bridger's GML, $g(\boldsymbol{x}; \boldsymbol{\phi}) \approx \frac{Q}{u_3 \widetilde{h}^{2.5}}$. This function is used to colour the data in Fig. 1b, scaled to units of µg/m$^{3.5}$. Visually, the colour gradient in the data from the top-left (high detection probability) to the bottom right (low detection probability) suggests strong correlation of this simple predictor with detectability.

Similar data are shown for the Kairos LeakSurveyor (Fig. 1c-d) and AVIRIS-NG (Fig. 1e-f) instruments. In contrast to Bridger's GML with
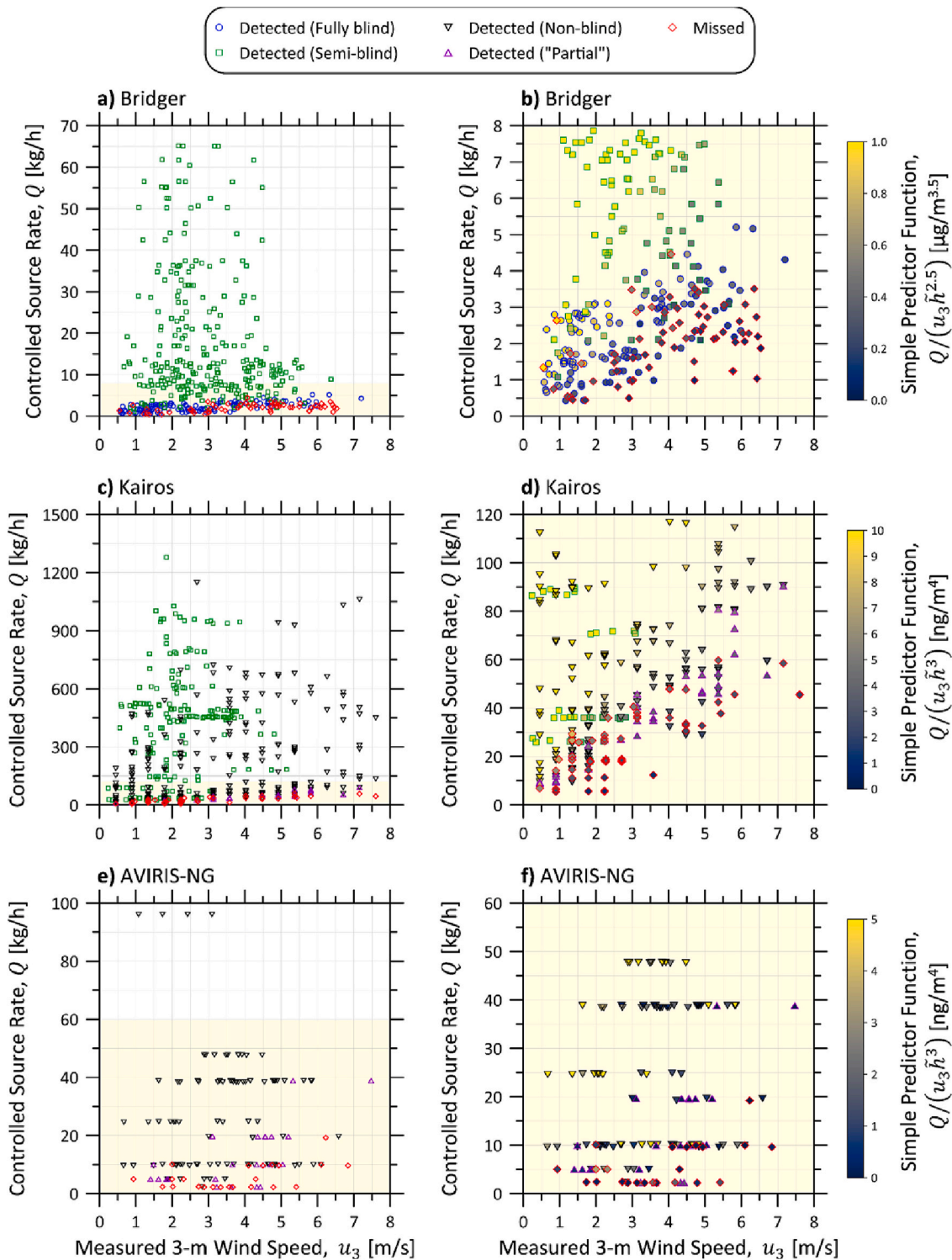
**Fig. 1.** Available controlled release data for (a,b) Bridger Photonics GML, (c,d) Kairos LeakSurveyor, and (e,f) AVIRIS-NG. Successful detections are outlined in blue (fully blinded data), green (semi-blinded data), or black (non-blinded data); partial detections in purple; and missed detections in red. Righthand panels (b, d, and f) show a zoomed subset of lower release rate data from the corresponding left panels, where the data points are also shaded according to each technique's simple predictor function (described in the main text) as outlined on the right of each panel. (For interpretation of the references to colour in this figure legend, the reader is referred to the web version of this article).

actively scanning optics, the detection sensitivity of these passive imaging spectrometers is expectedly lower, such that some emissions likely to be detected by Bridger may be missed by Kairos' LeakSurveyor or AVIRIS-NG. Additionally, for these imaging optics that can be approximated with a pinhole model, spatial resolution at the ground/plume is linear with aircraft altitude, implying that signal strength is proportional

to $\tilde{h}^{-1}$. Combining this with the inverse square law ($\tilde{h}^{-2}$) suggests that the equivalent *simple* prediction function these techniques should be $g(\boldsymbol{x};\boldsymbol{\phi}) \approx \frac{Q}{u_3 \tilde{h}^3}$, indicating a greater potential sensitivity to aircraft altitude than Bridger's GML. Fig. 1d and f show the controlled release data according to this latter predictor function in units of ng/m⁴ – recall

**Table 2**

Derived POD functions for GML, LeakSurveyor, and AVIRIS-NG, combining optimized predictor and inverse link functions. Detailed equations of the predictor and inverse link functions for each technology are summarized in Table S2 of the SI.

| Technology | Optimized Probability of Detection (POD) Function |
|---|---|
| Bridger Photonics Inc. Gas-mapping LiDAR (GML) | $POD = exp\left( -\left( \dfrac{0.224\, Q_{[kg/h]}^{1.07}}{\left(\frac{\tilde{h}_{[m]}}{1000}\right)^{2.44} \left(u_{3[m/s]} + 2.14\right)^{1.69}} \right)^{-2.53} \right)$ |
| Kairos Aerospace LeakSurveyor[a] *(Excluding Partial Detections)* | $POD = 1 - \left(1 + \left(\dfrac{\left(8.50\times 10^{-3}\right) Q_{[kg/h]}^{1.99}}{\left(u_{3[m/s]} + 0.534\right)^{1.92}}\right)^2\right)^{-1.5}$ |
| Kairos Aerospace LeakSurveyor[a] *(Including Partial Detections)* | $POD = 1 - \left(1 + \left(\dfrac{\left(7.71\times 10^{-3}\right) Q_{[kg/h]}^{1.87}}{\left(u_{3[m/s]}\right)^{1.41}}\right)^2\right)^{-1.5}$ |
| NASA JPL AVIRIS-NG *(Excluding Partial Detections)* | $POD = 1 - \left(1 + \left(\dfrac{\left(31.1\times 10^{-3}\right) Q_{[kg/h]}^{1.99}}{\left(\frac{\tilde{h}_{[m]}}{1000}\right)^{1.91} exp\left(0.239\, u_{3[m/s]}\right)}\right)^2\right)^{-1.5}$ |
| NASA JPL AVIRIS-NG *(Including Partial Detections)* | $POD = exp\left( -\left( \dfrac{0.365\, Q_{[kg/h]}^{1.10}}{\left(\frac{\tilde{h}_{[m]}}{1000}\right)^{0.731} exp\left(0.114\, u_{3[m/s]}\right)} \right)^{-2.53} \right)$ |

[a] Aircraft altitude during controlled release experiments of Kairos' LeakSurveyor did not deviate from the targeted aircraft altitude of 900 m AGL (approximately 3000 ft), so aircraft altitude is necessarily ignored in the stated POD function. The optimized model can theoretically be extended to other altitudes by forcing the exponent on aircraft altitude to its expected value of 3.0 and updating other coefficients as necessary. Note however that there are no public data to support model accuracy at other altitudes and this extrapolation should be performed with caution given the observed deviation of AVIRIS-NG's optimized predictor function from the same expected value of 3.0.

however, that available Kairos data were acquired at the single targeted altitude of 900 m AGL. Interestingly, in contrast to Bridger's GML, the gradient in this colouring scheme is less pronounced for AVIRIS-NG, indicating that detection sensitivity is not well-captured by the simple predictor model.

Although potentially useful, the simple predictor functions $g(x; \phi) \approx \frac{Q}{u_3 \tilde{h}^{2.5}}$ and $g(x; \phi) \approx \frac{Q}{u_3 \tilde{h}}$ in Fig. 1b, d, and f are sub-optimal since, in addition to being non-parametric and approximate, this formulation forces contours of constant POD to be linear and converge at the origin in the $Q$-$u_3$ domain. Thus, for a fixed aircraft altitude, this formulation results in the same non-physical POD at low wind speeds as the linear predictor model. To avoid this issue and to generalize the predictor model, the present analysis considers an optimizable model of the form:

$$g(x; \phi) = \phi_7 \frac{\left(Q_{[kg/h]} - \phi_1\right)^{\phi_3}}{\tilde{n}_{[ppm \cdot m]}^{\phi_4} \left(\frac{h_{[m]}}{1000}\right)^{\phi_5} \left(u_{3\left[\frac{m}{s}\right]} - \phi_2\right)^{\phi_6}} \quad (7)$$

where representative scene noise ($\tilde{n}$) has been introduced for completeness and may be optionally considered via optimization of coefficient $\phi_4$ and units of each variable have been explicitly stated in square brackets. Choosing $\phi_1 > 0$ and/or $\phi_2 < 0$ ensures a physically reasonable POD at zero-wind, unlike the linear prediction model and the simple, non-parametric predictor functions described above and used to colour data in Fig. 1b, d, and f. Similarly, non-negative exponents $\phi_{3-6}$ allow for deviation from linearity or, in the case of $\phi_5$ for aircraft altitude, from the simple predictor functions described above. Importantly, the generalized predictor model of Eq. (7) is non-negative and monotonically increases with source rate and decreases with scene noise, aircraft altitude, and 3-m wind speed. This means that candidate inverse link functions can take the form of the cumulative distribution function (CDF) of any distribution with non-negative support (e.g., lognormal, Fréchet, etc.).

As further detailed in the SI (see especially Table S1), the optimization considered a broad range of possible inverse link functions while independently testing the importance of each variable in Eq. (7).

Considering first the subset of controlled release measurements where scene noise data were available, in all instances the optimization showed that including either scene noise *or* aircraft altitude in the model, i.e., permitting $\phi_4$ *or* $\phi_5$ to be non-zero, was strongly statistically justified. By contrast, including both parameters was either not justified or only marginally justified ($\Delta AICc < \sqrt{10}$, see SI); that is, classed as "not worth more than a bare mention" (Kass and Raftery, 1995; Snipes and Taylor, 2014). Thus, given that aircraft altitude is a trivial parameter to quantify (and in the present case available for Bridger's GML as a standard output), the remainder of the POD derivation ignores scene noise, forcing $\phi_4 = 0$ and optimizing for the exponent on aircraft altitude, $\phi_5$.

Subsequent optimization was performed using all available controlled release data plotted in Fig. 1a for Bridger's GML ($N = 466$), Fig. 1c for Kairos' LeakSurveyor ($N = 582$), and AVIRIS-NG (Fig. 1f for AVIRIS-NG ($N = 139$). As an example, the best-fitting model for the GML data had the following optimized predictor function:

$$g\left(Q, u_3, \tilde{h}\right) = \frac{0.152\, Q_{[kg/h]}^{1.07}}{\left(\frac{\tilde{h}_m}{1000}\right)^{2.44} \left(u_{3[m/s]} + 2.14\right)^{1.69}} \quad (8)$$

and employed a Fréchet CDF for the inverse link function:

$$F(g) = exp\left(-0.372 g^{-2.53}\right) \quad (9)$$

Combined, these give the probability of detection for any specific source rate, wind speed, and altitude using Bridger's GML. Importantly, the generalized approach used to produce this detailed model can be readily extended to any other technology for which sufficient controlled release data are available. Using published controlled release data for Kairos' LeakSurveyor (Sherwin et al., 2021) and AVIRIS-NG (Thorpe et al., 2016) and additional internal controlled release data from Kairos, POD functions were derived for each of these technologies using the developed method. The final optimized POD functions, which combine the predictor and inverse link functions, are summarized for each technology in Table 2; optimized predictor functions are available in the SI. For
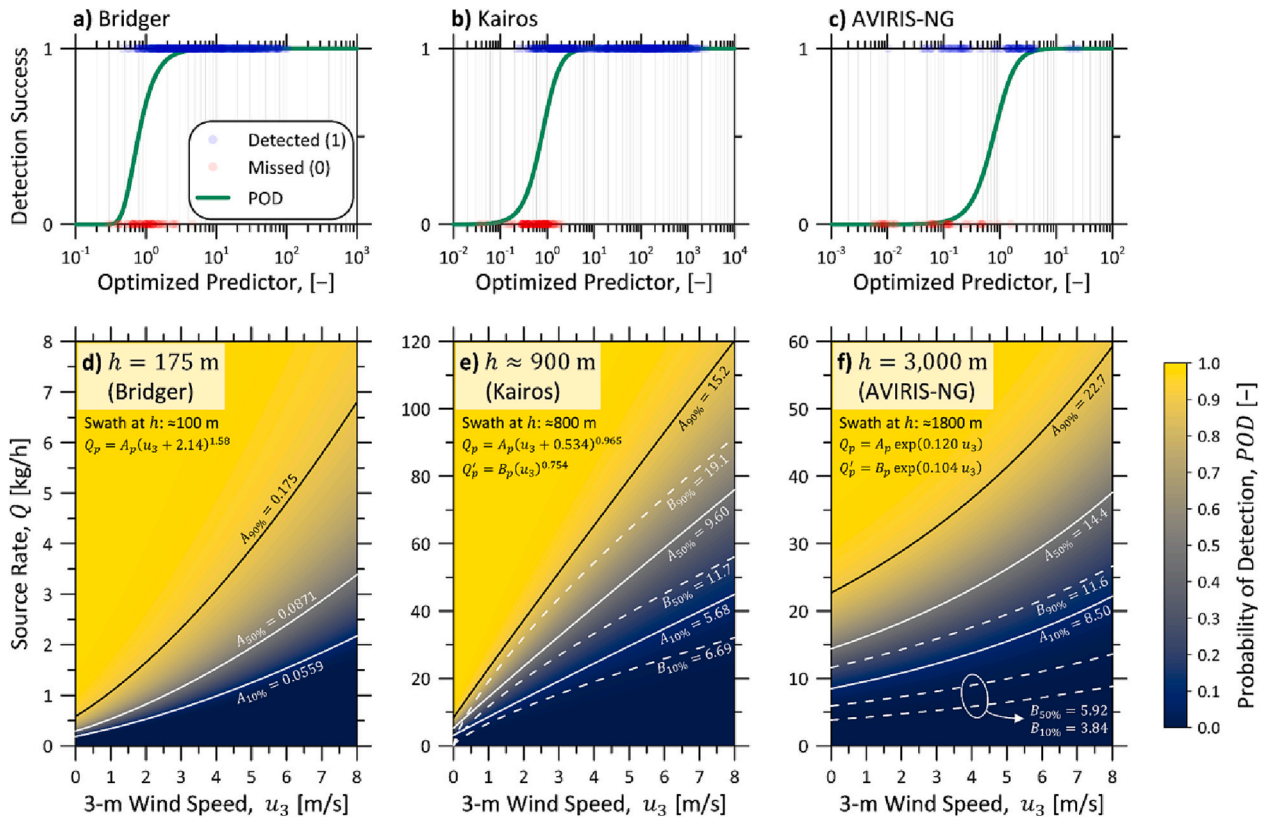
**Fig. 2.** Robustly derived probability of detection (POD) functions for Bridger's GML technology, Kairos' LeakSurveyor technology, and AVIRIS-NG. a-c) detection success against optimized predictor function values for all available controlled release data for each instrument alongside the corresponding optimized inverse link function (green line). d-f) calculated probability of detection as a function of source rate and 3-m wind speed at typical flight altitudes (corresponding approximate swath widths also shown) for each instrument. Contours for probabilities of detection of 10, 50, and 90% and their associated functions ($Q_p$) are overlaid in each plot as solid lines. For comparison, POD contours if partial detections are included are also plotted with their associated functions ($Q_p'$) as dashed lines. Table 2 provides general equations for POD as a function of source rate, wind speed, and altitude (where relevant) for all cases in this figure. (For interpretation of the references to colour in this figure legend, the reader is referred to the web version of this article).

both Kairos' LeakSurveyor and AVIRIS-NG cases, representative instrument noise data for the controlled releases were not available (hence, $\phi_4 = 0$). Additionally, for Kairos' LeakSurveyor, aircraft altitude was constant during controlled release experiments so the optimized exponent on aircraft altitude ($\phi_5$) was also necessarily ignored.

Optimization of the generalized predictor function in Eq. (8) using the controlled release data for Bridger's GML technology identified an optimal exponent on aircraft altitude ($\phi_5$) of 2.44, quite close to the theoretical/expected value of 2.5. By contrast, optimization of the AVIRIS-NG controlled release data yielded an optimal exponent on aircraft altitude of 0.731–1.91, which is lower than the expected value of 3.0 assuming simple pinhole optics. Given this deviation and noting that aircraft altitude was not varied from the targeted level in the controlled release studies of Kairos' Leak Surveyor, one should use caution if seeking to extrapolate from the presented POD function for Kairos to other altitudes.

Fig. 2a-c plots detection success against the value of the optimized predictor function for the controlled releases of Bridger's GML, Kairos' LeakSurveyor, and AVIRIS-NG, respectively. The optimized inverse link function is overlaid in each plot. Fig. 2d-f combines the optimized predictor and inverse link to display the POD function within the $Q$-$u_3$ domain at typical/common aircraft altitudes for Bridger's GML (175 m), Kairos' LeakSurveyor (900 m), and AVIRIS-NG (3000 m, Duren et al., 2019; Thorpe et al., 2021), respectively. Contours at probabilities of detection of 10, 50, and 90% – and the associated functions, $Q_p$ – are also plotted as solid lines. The dashed lines (and associated functions, $Q_p'$) show the POD if partial (human-identified) detections are included in the analyses of Kairos' LeakSurveyor and AVIRIS-NG and treated equally as algorithmic detections.

The POD functions plotted in Fig. 2d-f and summarized in Table 2 provide continuous detection probabilities on a *measurement-specific* basis for any given wind speed, source rate, and altitude. These functions have not existed to date and are precisely what is required for realistic analysis using emissions abatement simulators like FEAST (Kemp et al., 2016) and modelling efforts supporting alt-FEMP applications. In FEAST for example, detection sensitivity has to date been treated as a binary variable with successful detection assumed if an instrument's sensitivity is exceeded by the maximum plume concentration estimated from Gaussian plume dispersion theory. This approach inherently ignores the continuous nature of detection probability and assumes idealized plume dispersion that is not supported by the data. The continuous POD functions developed in this work identify non-linear sensitivities to source rate size and measurement conditions and can be readily implemented within FEAST and other models to probabilistically assess detection success. Similarly, robust POD data are vital for objective analysis of missed detections in situations where multiple measurements are made over the same facility.

As expected, and noting the different scales in Fig. 2d-f, the detection sensitivities of Bridger's active sensor are much lower than either of the passive sensors. Considering typical altitudes of 175, 900, and 3000 m AGL (corresponding to approximate measurement swaths of 100, 800, and 1800 m) for each technology respectively, at a common reference wind speed of 3 m/s, the controlled release data identify that Bridger's GML might be expected to detect single sources of 1.2 kg/h in size at 50% probability, Kairos a 27/32 kg/h source, and AVIRIS-NG a 8.1/21 kg/h source (the latter two lower/upper values depending on whether partial, human-reviewed detections are considered as detections or not).

At 90% detection probability, these thresholds become 2.3 kg/h, 44/51 kg/h, and 16/33 kg/h, respectively. At an aircraft altitude of 8000 m AGL, the upper limit of flights in a recent study (Thorpe et al., 2021), the 50% and 90% detection thresholds for AVIRIS-NG are 15/53 kg/h and 30/84 kg/h, respectively, although estimates for this altitude are necessarily extrapolated from the available published data which includes releases for flight altitudes up to 3800 m AGL. At fixed altitudes, the optimized POD functions for all three technologies provide physically realistic non-zero intercepts at zero wind speed when ignoring partial detections. These contours contrast with assumed detection sensitivities or partial detection ranges with non-physical zero-intercepts based on wind-normalized source rates (Berman et al., 2021; Chen et al., 2022; Sherwin et al., 2021; Bell et al., 2022) as well as the assumed linear model of Johnson et al. (2021) for Bridger's GML. Fig. S4 of the SI compares the newly derived continuous POD functions with these previously published detection sensitivities for each technology. There is a slight improvement in the detection sensitivity of Bridger's GML over that estimated from limited tests in the 2019 data of Johnson et al., 2021. Detection sensitivities are of similar magnitude for Kairos' LeakSurveyor as in Sherwin et al.'s (2021) and Berman et al.'s (2021) analyses. Likewise, the present approach overlaps significantly with Thorpe et al.'s (2016) stated partial detection range, however the new result improves upon this by parameterizing the POD with wind speed and aircraft altitude.

The optimized POD function for Kairos' LeakSurveyor is approximately linear with wind speed when ignoring partial detections. While this result is justified by goodness-of-fit statistics, subjective inclusion/exclusion of data can yield significantly different results. Using this technology as an example and referring to Fig. S5 in the SI, POD contours are strongly super-linear if Sherwin et al.'s (2021) data are considered alone (Fig. S5a) but, by contrast, become approximately linear if only Kairos' internal data are considered (Fig. S5b). When combining these unique data sets, the optimized POD function biases toward the former and yields contours that are approximately linear (Fig. 2e and S5c). This sensitivity to data inclusion is likely due to the scarcity of data near the sensitivity limit in Sherwin et al.'s (2021) experiments (see Fig. S5a in the SI). For instance, one-minute-averaged 3-m wind speeds during Sherwin et al.'s (2021) experiments did not exceed 5.5 m/s as compared to maximum wind speeds of 7.4 m/s in the Bridger GML and > 8.0 m/s in the AVIRIS-NG controlled release data. Moreover, due to instrumentation constraints noted by Sherwin et al. (2021), releases near the sensitivity limit were occasionally held constant during consecutive (up to 16) flight passes, letting the variable wind perturb detectability of the plume. Consequently, the available controlled release data tend to be clustered in the $Q - u_3$ domain, such that a POD function for Kairos' LeakSurveyor derived from Sherwin et al.'s (2021) data alone should not be extrapolated. Nevertheless, the observed sensitivity of the optimized POD function to the contributing datasets supports the continued acquisition (and public sharing) of controlled release data for these technologies.

The controlled release data for AVIRIS-NG resulted in optimized POD functions with large values of $\phi_2$. This coefficient, which translates the wind speed coordinate in the predictor and POD functions, optimized toward negative infinity as $\phi_1$ and $\phi_6$ optimized toward positive infinity. It is unclear whether this is a consequence of the plume segmentation algorithm employed by Thorpe et al. (2016) or their experimental approach to the controlled releases. Given this result, at the optimum, the predictor function for the AVIRIS-NG instrument can be more concisely written than Eq. (7) by replacing $(u_3 - \phi_2)^{\phi_6}$ with $\exp(\phi_2' u_3)$ as shown in the final optimized POD functions of Table 2. This formulation avoids potential issues with numerical resolution and improves convergence during optimization. Considering this specific observation, but also the POD analysis more generally, it is important to note that optimized coefficients are fundamentally empirical in nature; caution should be used in interpreting/comparing fitted coefficients, which are sensitive not just to the underlying data, but also the specific form of the

best-fitting predictor and inverse link functions identified for each technology.

As presented, the derived POD models assume accurate knowledge of aircraft altitude and 3-m wind speed. This is the appropriate form when trying to understand what might be detectable in a range of field study scenarios and/or modelling of alternate fugitive emissions management programs (Alt-FEMP) or alternative means of emission limitation (AMEL) proposals. However, when interpreting data from a specific field campaign, accurate in-situ wind data are generally not available and database/modelled wind speed at some arbitrary height above ground level ($z$) must instead be used to infer the POD. This scenario necessarily requires an error model for the wind speed and, if $z \neq 3$ m, an assumed vertical wind speed profile. Such a model is likely to be highly dependent on time and location as well as the source of the wind speed estimate and ideally should be derived from data relevant to any particular measurement campaign. However, if a wind error model of the form $\pi\left(u_3 | \widetilde{u}_z\right)$ exists (i.e., a conditional distribution of the true 3-m wind speed given the available estimate at $z$ – i.e., $\widetilde{u}_z$), then the POD can be readily quantified considering bias/precision in the estimated wind speed via:

$$\text{POD}\left(Q, \widetilde{u}_z, \widetilde{h}\right) = \int_0^\infty \text{POD}\left(Q, u_3, \widetilde{h}\right) \pi\left(u_3 | \widetilde{u}_z\right) du_3 \qquad (10)$$

Wind speed error distributions from a reference 3-m height $\pi\left(u_3 | \widetilde{u}_3\right)$, were derived using available wind data from the controlled release trials of Bridger's GML and Kairos' LeakSurveyor. The resulting distributions, optimized in the same manner as the quantification error distributions, are summarized in Table S4 of the SI and can be used with the optimized POD functions in Table 2 to compute probabilities of detection given *estimated* wind speed via Eq. (10).

### 4.2. Source quantification uncertainty

Fig. 3a and b compare the known ($Q$) and estimated ($\widetilde{Q}$) source rates across the controlled release studies of Bridger's GML and Kairos' LeakSurveyor technologies. Estimated source rates for Bridger's GML technology were taken directly from their reported results; all 284 non-zero, semi-blinded, high-flowrate releases in the 2020 and 2021 campaigns are shown in Fig. 3a alongside a 1:1 parity line. Fig. 3b plots similar data from Sherwin et al.'s (2021) external controlled release experiments and Kairos' internal experiments of its LeakSurveyor, where data correspond to all detected controlled releases >50 kg/h and without any identified quality control concerns. Source rates were computed from Kairos' estimated wind-normalized source rates and multiplied by modelled wind speed at 3-m height above ground. Four datasets are shown in Fig. 3b corresponding to wind data from Dark Sky – one-minute average (green) and gust (yellow) – and HRRR – one-hour average (red) and gust (blue). Recognizing that quantification errors scale with source rate, Fig. 3c plots the resulting probability distributions for the *relative* error ratio (RER $= Q/\widetilde{Q}$) from the data in Fig. 3a and b according to Eq. (6), which ignores potential site-to-site and day-to-day variability in measurement accuracy; means of each distribution, representing overall measurement biases, are identified by points. Bridger's GML estimates using Meteoblue wind data and Kairos' LeakSurveyor estimates using one-minute *gust* data from Dark Sky show minimal bias errors, with relative error ratios of 0.92 and 1.07, respectively. By contrast, bias errors can be larger (1.34) when using one-hour gust wind data from HRRR and prohibitively large using one-minute *average* Dark Sky or one-hour *average* HRRR data (2.14 and 2.53, respectively) with Kairos' LeakSurveyor technology. Table 3 summarizes key statistics (mean, median, and 95% equal tail confidence intervals) for each of these distributions shown in Fig. 3c and Table S3 of
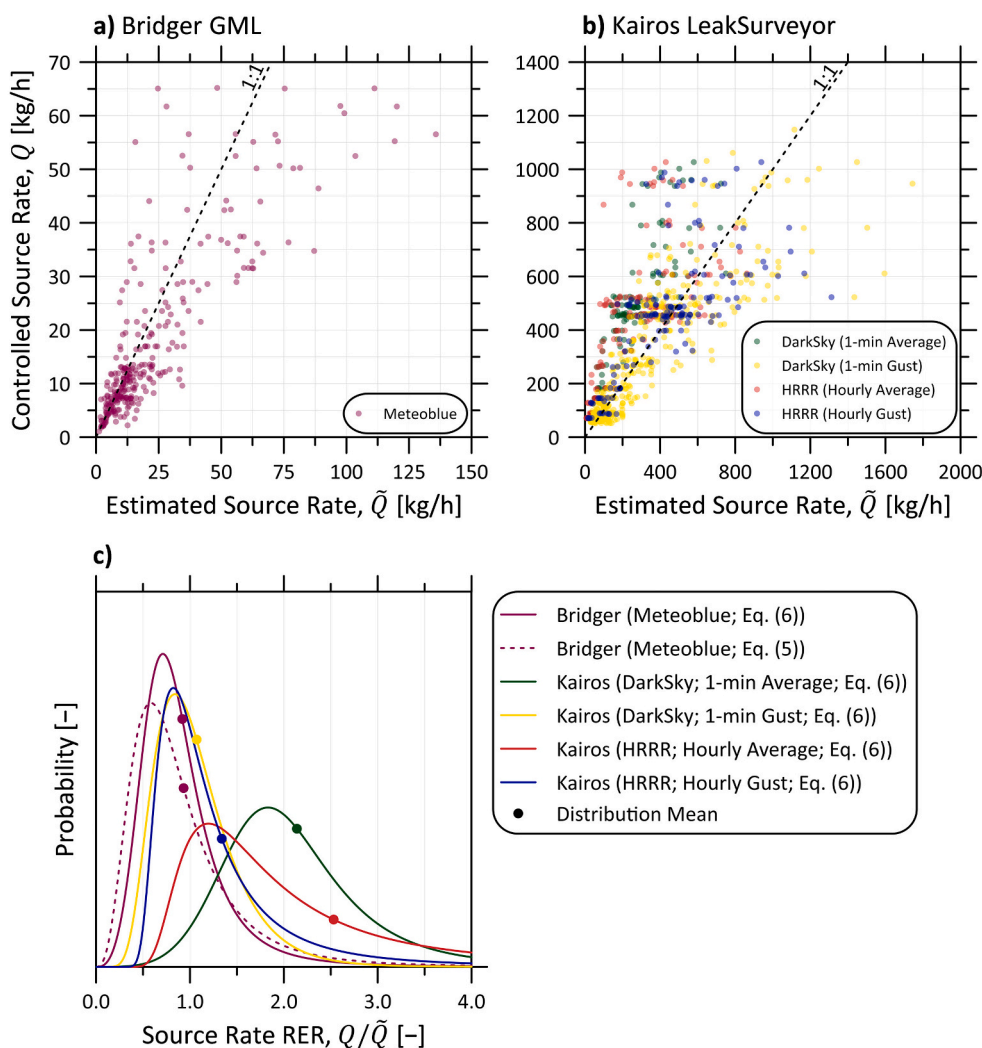
**Fig. 3.** Summary of controlled release data and quantification error analysis for a) Bridger's GML technology using Meteoblue wind data (purple) and b) Kairos' LeakSurveyor technology, computed using Dark Sky one-minute average (green) and gust (yellow) and HRRR hourly average (red) and gust (blue) wind data. (c) Resulting distributions of the source rate relative error ratio (RER) for each technique and wind source via fitting of Eq. (6) in addition to the source rate RER for Bridger's GML technology using Eq. (5). Distribution means, representing quantification bias error are identified for each distribution by a point. (For interpretation of the references to colour in this figure legend, the reader is referred to the web version of this article).

**Table 3**

Statistics of the relative error ratio (RER $= Q/\widetilde{Q}$) for Bridger's GML and Kairos' LeakSurveyor technologies; source data corresponds to the high-flowrate (1–66 kg/h) controlled releases from the present study and all valid controlled releases > 50 kg/h from Sherwin et al. (2021) and Kairos' internal experiments. RER statistics (mean, median, and 95% equal tail confidence interval (CI)) are shown for each technique and, for Kairos' LeakSurveyor, when using different sources of wind speed data.

| Instrument | Wind Source | Wind Statistic | Mean (Bias) | Median | 95% Equal Tail CI |
|---|---|---|---|---|---|
| Bridger GML | Meteoblue | Proprietary | 0.92 | 0.82 | 0.31–2.13 |
| Kairos LeakSurveyor | Dark Sky | 1-min Gust | 1.07 | 0.99 | 0.45–2.17 |
| | | 1-min Average | 2.14 | 1.99 | 0.94–4.23 |
| | HRRR | 1-h Gust | 1.34 | 1.07 | 0.57–3.74 |
| | | 1-h Average | 2.53 | 1.74 | 0.77–8.82 |
| | In Situ | 1-min Gust | 0.99 | 0.92 | 0.45–1.88 |
| | | 1-min Average | 1.38 | 1.29 | 0.60–2.74 |

the SI provides detailed equations for the conditional probability distribution, $\pi\left(Q\,|\,\widetilde{Q}\right)$, for each combination of technology and wind speed data source. These distributions are the essential inputs for Monte Carlo methods enabling comprehensive uncertainty analysis in large measurement campaigns that specifically include aggregation of detected

sources to develop measurement-based inventories (e.g., Johnson et al., 2023; Tyner and Johnson, 2021). Importantly, such measurement campaigns may also include multi-pass measurements of single sources/facilities; the presented distributions can be used to predict and calculate quantification uncertainties to support survey design and data analysis in this multi-pass context. Using Bridger's GML as an example, the quantification error model via Eq. (6) suggests the 95% equal tail confidence interval of the RER for a single pass is 0.31–2.13, which narrows to 0.56–1.52 after just four flight passes.

The improved quantification accuracy when using *gust* instead of *average* wind speeds to estimate source rate with Kairos' LeakSurveyor is somewhat counterintuitive since average wind speed is more indicative of the history of plume propagation prior to any observation. This seemingly anomalous observation could be a result of the coarse spatiotemporal resolution in database/modelled winds, which might tend to underestimate averages of non-negative and right-skewed wind speeds. However, this is much more likely related to how Kairos' wind-normalized source rate is estimated based on a defined "core" of the plume. Specifically, Kairos estimates wind-normalized source rate by dividing the total observed excess methane mass in the "core" of the plume by the length of this plume "core" in the direction of the wind; to then estimate source rate, this parameter is multiplied by the estimated wind speed. This is equivalent to averaging the flux of methane through control surfaces orthogonal to and spanning the length of the plume core. This approach is only valid in the case of infinite sensitivity where excess methane at the edges of the plume is fully resolved. In practice

though, finite sensitivity implies that the excess mass of methane in the plume is inherently underestimated, and this effect is accentuated by constraining the analysis to an arbitrary plume core. To overcome this underestimation of plume mass, an upward correction to wind speed would be necessary. This same result has been identified for satellite-based methane detection methods – particularly the cross-sectional flux (CSF) method (e.g. Varon et al., 2018 and references therein), which is similar to Kairos' approach. Robust analyses of this quantification method in the context of satellite remote sensing confirms that database/modelled average wind speeds must be calibrated/corrected to accurately recover known source rates. The calibration correction has been found to be sensor noise- and plume-dependent and studies have estimated it to range from +30 to +75% for satellite instruments (Jervis et al., 2021; Varon et al., 2020). Recognizing that database/modelled wind speeds are inherently biased and uncertain, it is possible and perhaps likely that the upward correction used to estimate gust wind speed from an average wind speed tends to mimic this required calibration correction.

To explore this further, Table 3 shows RER statistics for Kairos' LeakSurveyor using in-situ wind speed data from Sherwin et al. (2021) and Kairos' internal controlled release studies. One-minute-averaging of in-situ wind speed tends to underestimate the true source rate (RER of 1.38), corresponding to a +38% calibration correction needed to minimize bias; this is consistent with published corrections needed for satellite imagery using the CSF method (Jervis et al., 2021; Varon et al., 2020). However, the in-situ, one-minute gust wind speed compensates for this underestimation (RER of 0.99). Thus, in this specific example, if wind-normalized source rate is derived using Kairos' plume "core", then the one-minute gust wind speed empirically minimizes bias.

### 4.2.1. Spatiotemporal variability of measurement bias

Use of the simpler error model shown in Eq. (6) assumes that site-to-site and day-to-day bias in measurement error for a given technique is negligible. While this is a necessary assumption if controlled release data are limited to few locations/days, it is also simplistic. For example, drift in optical components and general atmospheric conditions may influence day-to-day variability in quantification accuracy, while localized conditions such as wind direction/turbulence and ground albedo can affect site-to-site variability. To glean insight into this bias variability, an additional analysis was performed using the present controlled release data for Bridger's GML technology, which includes releases from four oil and gas sites recorded over multiple days in two field campaigns one year apart. Fig. 4a presents a box-whisker diagram for the relative error ratio (RER) of the Bridger GML-estimated source rate, which takes the 284 controlled releases and computes statistics for data aggregated by measurement day (eight days spanning 2020 and 2021) and site (four locations). In these diagrams the central bar represents the interquartile range (25th to 75th percentile), the gray bars extend to the 90% equal tail confidence interval (CI), and the red crosses indicate extreme data outside the 90% CI. The central bars are notched at the mean value of the aggregated data, which represents bias for a specific measurement day or location. Measurement bias (quantified as the mean source rate RER at a particular site or on a particular measurement day) varied moderately on a site-by-site basis, from 0.89 to 0.99, and significantly on a day-to-day basis, from 0.53 to 1.74. This implies that bias on any one day and/or at any one site can be significant; however, available data also imply that, on average, bias across multiple days/sites is not statistically different than unity at a 5% significance level.

Fig. 4b provides insight into the source of bias variability by showing the same box-whisker diagrams for the RER in modelled 3-m wind speed from Meteoblue (used in Bridger's quantification) vs. the actual measured wind speed. As evidenced by these figures, day-to-day bias errors in estimated source rate correlate with the errors in the modelled 3-m wind speed ($\rho = 0.974$), implying that source rate bias on a day-to-day basis is driven by error in the windspeed. By contrast, source rate and wind speed bias are negligibly correlated on a site-by-site basis ($\rho = 0.048$). This implies that, at least for the present dataset, site-specific sources of bias like surface albedo and site infrastructure that affects wind speed error may be unimportant relative to day-to-day variability in wind speed error.

Thus, while Eq. (6) is the only practical error model when constrained by limited controlled released data, Eq. (5) is preferred to avoid underestimation of uncertainties given the potential significance of day-to-day variability in measurement bias. The difference between these approaches is demonstrated in Fig. 3c, where the present controlled release data for Bridger's GML from four sites over eight unique days in two different years is sufficient to model uncertainties via either Eq. (5) or (6). Use of Eq. (5) in place of the simplified Eq. (6) yielded no meaningful effect on the average bias, which changed <1.5%. However, as shown in the figure, and expected given the proper consideration of bias variability, Eq. (5) estimates higher dispersion in source rate RER (33% increase in standard deviation of RER) than Eq. (6). This increased variability when considering day- and site-dependent bias is moderate but not insignificant, and implies an underestimation of quantification uncertainty if controlled release data are limited to a small number of locations and/or measurement days and Eq. (6) is used for quantification error analysis. Based on these results, it is highly recommended that future controlled release studies be completed from a range of unique locations and over as many different days as feasible.
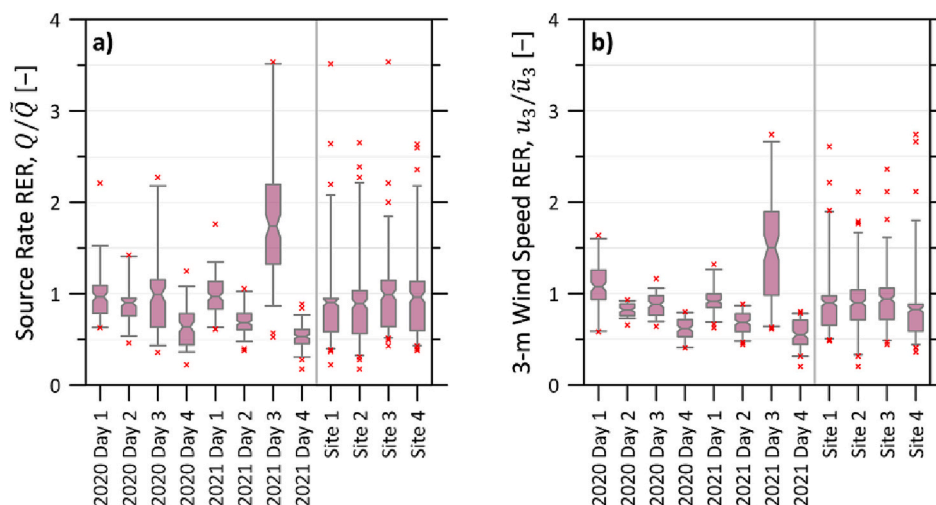


**Fig. 4.** Box-whisker diagrams for the relative error ratio (RER) of source rate using Bridger's estimates with Meteoblue wind data, accumulated by measurement day (a) and site (b). The central bars of the box-whisker diagrams are notched at the mean error (i.e., bias) and span the interquartile range; whiskers correspond to the 90% equal tail confidence interval (CI) and red crosses mark extreme data outside the 90% CI. Day-to-day variability is significant with bias errors ranging from 0.53 to 1.74. (For interpretation of the references to colour in this figure legend, the reader is referred to the web version of this article).

*4.3. Limitations*

The methodology presented in this manuscript permits derivation of physically realistic and continuous POD functions and robust quantification error models for aerial methane measurement technologies. The application of these new methods to the three example technologies provides informative results for use in other studies but are inherently specific to the data available at the time of publication.

Depending on the design of existing controlled release experiments, available data may be insufficient to fully resolve the sensitivities of the POD function and quantification error model to source location (i.e., terrain and landcover) and measurement date (i.e., weather conditions and optical drift). As identified in Section 4.2.1, site-to-site and day-to-day variability in quantification bias can be significant and future studies should strive to perform experiments at a variety of sites/locations over as many days as feasible to permit construction of error models via Eq. (5). Moreover, Section S3 the SI, which includes a comparison of the optimized POD function for Kairos' LeakSurveyor using only semi- or only non-blinded detections, identifies the need for future third-party studies that focus on rigorous experimental blinding; this is especially needed for the passive imaging spectrometers. Lastly, to maximize the accuracy of any empirical model it is important that controlled release experiments are performed in realistic situations. This includes releases among active oil and gas infrastructure that influence the complex wind field driving plume propagation and may introduce confounding emissions that affect (reduce or enhance) the ability to detect and accurately quantify sources with overlapping plumes.

## 5. Conclusions

Generalized models to characterize probabilities of detection and quantification error were developed and applied to three aerial methane-detection technologies: Bridger Photonics Inc.'s Gas-Mapping LiDAR (GML), Kairos Aerospace's LeakSurveyor, and the (U.S.) National Aeronautic and Space Administration's Jet Propulsion Laboratory's Next-Generation Airborne Visible/Infrared Imaging Spectrometer (AVIRIS-NG). Leveraging binary regression with a generalized predictor function, this new method improves upon existing techniques in the literature by enabling derivation of continuous and physically realistic POD functions that are variable on methane source rate, ambient wind speed, and aircraft altitude (where available). POD functions optimized to available controlled release data identified technology-specific detection sensitivities that vary with wind speed and altitude. At typical/target aircraft altitudes and a representative average wind speed of 3 m/s, Bridger's GML, Kairos' LeakSurveyor, and AVIRIS-NG were predicted to identify methane emissions of 2.3, 44/51, and 16/33 kg/h with 90% probability, respectively, where the latter two lower/upper values depend on whether partial, human-reviewed detections are considered as detections or not).

Using a subset of controlled release data for Bridger's GML and Kairos' LeakSurveyor that included source rate estimates for comparison with ground truth, controlled source rates, quantification uncertainties were separately characterized, including analysis of effects of using four optional database sources of wind speed for Kairos' LeakSurveyor. The developed statistical model permits analysis of measurement bias, *variability* in measurement bias (where data permit), and measurement precision, where the latter two are treated as probabilistic variables. Using the Meteoblue wind speed data product, the source rate relative error ratio (RER – i.e., actual over estimated source rate) for Bridger's GML averaged to 0.92 with a 95% confidence interval of 0.31–2.13. The analysis of Kairos' LeakSurveyor identify that source rate RER was highly sensitive to the wind speed data source and statistic (i.e., gust vs. average wind speed) and gust wind speed provided significantly less-biased results. One-minute gust wind speed from the Dark Sky database and one-hour gust wind speed from the HRRR database yielded mean source rate RERs of 1.07 and 1.34 with 95% confidence intervals

of 0.45–2.17 and 0.57–3.74, respectively. Data from the present controlled release study of Bridger's GML demonstrated that day-to-day variability in measurement bias was strongly correlated with wind speed error and appreciably increased the dispersion of the source rate RER. These results identify the need to target an assortment of different measurement locations and maximize measurement days during future controlled release studies.

Ultimately, the described methods – successfully applied to three example technologies – yield the robustly derived continuous POD function and probabilistic quantification error model that are needed to properly simulate emissions abatement/reduction and support methane monitoring, reporting, and verification via aircraft-based remote sensing. Moreover, the developed generalized methods are readily extensible to analysis of other remote sensing techniques or can be used to update POD and uncertainty models as further controlled release data become publicly available.

## CrediT author statement

All authors conceptualized the research and developed the methodology. MJ was responsible for funding acquisition, project administration, provision of resources, and supervision. BC and DT curated the data and performed the formal analysis and investigation. BC developed the software. All authors produced the original manuscript including visualizations and reviewed and edited the manuscript throughout the publication process.

## Declaration of Competing Interest

The authors declare that they have no known competing financial interests or personal relationships that could have appeared to influence the work reported in this paper.

## Data availability

Non-confidential data will be posted or shared upon request

# Appendix A. Supplementary data

Supplementary data to this article can be found online at https://doi.org/10.1016/j.rse.2023.113499.

# References

AER, 2021. Alternative Fugitive Emission Management Program Approvals [WWW Document]. URL. https://www.aer.ca/protecting-what-matters/holding-industry-accountable/industry-performance/methane-performance/alternative-fugitive-emission-management-program-approvals (accessed 2.15.21).

Apple Inc., 2022. Dark Sky API [WWW Document]. URL. https://darksky.net/dev (accessed 6.9.22).

Arias, P.A., Bellouin, N., Coppola, E., Jones, R.G., Krinner, G., Marotzke, J., Naik, V., Palmer, M.D., Plattner, G.-K., Rogelj, J., Rojas, M., Sillmann, J., Storelvmo, T., Thorne, P.W., Trewin, B., Rao, K.A., Adhikary, B., Allan, R.P., Armour, K., Bala, G., Barimalala, R., Berger, S., Canadell, J.G., Cassou, C., Cherchi, A., Collins, W., Collins, W.D., Connors, S.L., Corti, S., Cruz, F., Dentener, F.J., Dereczynski, C., Di Luca, A., Niang, A.D., Doblas-Reyes, F.J., Dosio, A., Douville, H., Engelbrecht, F., Eyring, V., Fischer, E., Forster, P., Fox-Kemper, B., Fuglestvedt, J.S., Fyfe, J.C., Gillett, N.P., Goldfarb, L., Gorodetskaya, I., Gutierrez, J.M., Hamdi, R., Hawkins, E., Hewitt, H.T., Hope, P., Islam, A.S., Jones, C., Kaufman, D.S., Kopp, R.E., Kosaka, Y., Kossin, J., Krakovska, S., Lee, J.-Y., Li, J., Mauritsen, T., Maycock, T.K., Meinshausen, M., Min, S.-K., Monteiro, P.M.S., Ngo-Duc, T., Otto, F., Pinto, I., Pirani, A., Raghavan, K., Ranasinghe, R., Ruane, A.C., Ruiz, L., Sallée, J.-B., Samset, B.H., Sathyendranath, S., Seneviratne, S.I., Sörensson, A.A., Szopa, S., Takayabu, I., Tréguier, A.-M., van den Hurk, B., Vautard, R., von Schuckmann, K., Zaehle, S., Zhang, X., Zickfeld, K., 2021. Technical summary. In: Masson-Delmott, V., Zhai, P., Pirani, A., Connors, S.L., Péan, C., Berger, S., Caud, N., Chen, Y., Goldfarb, L., Gomis, M.I., Huang, M., Leitzell, K., Lonnoy, E., Matthews, J.B.R., Maycock, T.K., Waterfield, T., Yelekçi, O., Yu, R., Zhoue, B. (Eds.), Climate Change 2021: The Physical Science Basis. Contribution of Working Group I to the Sixth Assessment Report of the Intergovernmental Panel on Climate Change. Cambridge University Press, pp. 33–144. https://doi.org/10.1017/9781009157896.002.

ARPA-E, 2018. Impact Sheet - Bridger Photonics (MONITOR) [WWW Document]. URL. https://arpa-e.energy.gov/impact-sheet/bridger-photonics-monitor (accessed 5.23.22).

Bell, C., Rutherford, J., Brandt, A., Sherwin, E., Vaughn, T., Zimmerle, D., 2022. Single-blind determination of methane detection limits and quantification accuracy using aircraft-based LiDAR. Elem. Sci. Anthr. 10 (1), 1–12. https://doi.org/10.1525/elementa.2022.00080.

Bell, C., Vaughn, T.L., Zimmerle, D.J., 2020. Evaluation of next generation emission measurement technologies under repeatable test protocols. Elem. Sci. Anth 8, 32. https://doi.org/10.1525/elementa.426.

Berman, Elena S.F., Wetherley, Erin B., Jones, Brian B., 2021. Kairos Aerospace Technical White Paper: Methane Detection (Version 1F). Kairos Aerospace. https://doi.org/10.17605/OSF.IO/HZG52.

Branson, K., Jones, B.B., Berman, E.S.F., 2021. Methane Emissions Quantification (No. Version 2). Kairos Aerospace, Mountain Vew, CA.

Bridger Photonics, 2021. Why is it Important that ExxonMobil Submitted Gas Mapping LiDAR™ for EPA Approval?. Available at https://www.bridgerphotonics.com/blog/why-is-it-important-exxonmobil-submitted-gas-mapping-lidar-epa-approval. (accessed 2.14.23).

Bridger Photonics, 2021. Gas Mapping LiDARTM [WWW Document]. URL. https://www.bridgerphotonics.com/gas-mapping-lidar (accessed 5.31.21).

CCAC, 2021. Global Methane Pledge [WWW Document]. URL. https://www.globalmethanepledge.org/ (accessed 4.28.22).

Chen, Y., Sherwin, E.D., Berman, E.S.F., Jones, B.B., Gordon, M.P., Wetherley, E.B., Kort, E.A., Brandt, A.R., 2022. Quantifying regional methane emissions in the New Mexico Permian Basin with a comprehensive aerial survey. Environ. Sci. Technol. 56, 4317–4323. https://doi.org/10.1021/acs.est.1c06458.

Cusworth, D.H., Jacob, D.J., Varon, D.J., Chan Miller, C., Liu, X., Chance, K., Thorpe, A. K., Duren, R.M., Miller, C.E., Thompson, D.R., Frankenberg, C., Guanter, L., Randles, C.A., 2019. Potential of next-generation imaging spectrometers to detect and quantify methane point sources from space. Atmos. Meas. Tech. 12, 5655–5668. https://doi.org/10.5194/amt-12-5655-2019.

Cusworth, D.H., Duren, R.M., Thorpe, A.K., Tseng, E., Thompson, D., Guha, A., Newman, S., Foster, K.T., Miller, C.E., 2020. Using remote sensing to detect, validate, and quantify methane emissions from California solid waste operations. Environ. Res. Lett. 15 https://doi.org/10.1088/1748-9326/ab7b99.

Cusworth, D.H., Duren, R.M., Thorpe, A.K., Olson-Duvall, W., Heckler, J., Chapman, J. W., Eastwood, M.L., Helmlinger, M.C., Green, R.O., Asner, G.P., Dennison, P.E., Miller, C.E., 2021. Intermittency of large methane emitters in the Permian Basin. Environ. Sci. Technol. Lett. 8, 567–573. https://doi.org/10.1021/acs.estlett.1c00173.

Duren, R.M., Thorpe, A.K., Foster, K.T., Rafiq, T., Hopkins, F.M., Yadav, V., Bue, B.D., Thompson, D.R., Conley, S., Colombi, N.K., Frankenberg, C., McCubbin, I.B., Eastwood, M.L., Falk, M., Herner, J.D., Croes, B.E., Green, R.O., Miller, C.E., 2019. California's methane super-emitters. Nature 575, 180–184. https://doi.org/10.1038/s41586-019-1720-3.

Elder, C.D., Thompson, D.R., Thorpe, A.K., Hanke, P., Walter Anthony, K.M., Miller, C.E., 2020. Airborne mapping reveals emergent power law of Arctic methane emissions. Geophys. Res. Lett. 47 https://doi.org/10.1029/2019GL085707.

EMNRD, 2023. Methane Waste Rule: Approved ALARM Technologies. New Mexico Energy, Minerals and Natural Resources Department (ENMRD). Available at. https://www.emnrd.nm.gov/ocd/methane-waste-rule/ (accessed 2.14.23).

European Commission, 2021. Proposal for a Regulation of the European Parliament and of the Council on Methane Emissions Reduction in the Energy Sector and Amending Regulation (EU) 2019/942. European Commission, Brussels.

Foote, M.D., Dennison, P.E., Thorpe, A.K., Thompson, D.R., Jongaramrungruang, S., Frankenberg, C., Joshi, S.C., 2020. Fast and accurate retrieval of methane concentration from imaging spectrometer data using sparsity prior. IEEE Trans. Geosci. Remote Sens. 58, 6480–6492. https://doi.org/10.1109/TGRS.2020.2976888.

Fox, T.A., Barchyn, T.E., Risk, D., Ravikumar, A.P., Hugenholtz, C.H., 2019. A review of close-range and screening technologies for mitigating fugitive methane emissions in upstream oil and gas. Environ. Res. Lett. 14, 053002 https://doi.org/10.1088/1748-9326/ab0cc3.

Frankenberg, C., Thorpe, A.K., Thompson, D.R., Hulley, G., Kort, E.A., Vance, N., Borchardt, J., Krings, T., Gerilowski, K., Sweeney, C., Conley, S.A., Bue, B.D., Aubrey, A.D., Hook, S., Green, R.O., 2016. Airborne methane remote measurements reveal heavytail flux distribution in Four Corners region. Proc. Natl. Acad. Sci. U. S. A. 113, 9734–9739. https://doi.org/10.1073/pnas.1605617113.

Green, R.O., Eastwood, M.L., Sarture, C.M., Chrien, T.G., Aronsson, M., Chippendale, B. J., Faust, J.A., Pavri, B.E., Chovit, C.J., Solis, M., Olah, M.R., Williams, O., 1998. Imaging spectroscopy and the airborne visible/infrared imaging spectrometer (AVIRIS). Remote Sens. Environ. 65, 227–248. https://doi.org/10.1016/S0034-4257(98)00064-9.

Guha, A., Newman, S., Fairley, D., Dinh, T.M., Duca, L., Conley, S.C., Smith, M.L., Thorpe, A.K., Duren, R.M., Cusworth, D.H., Foster, K.T., Fischer, M.L., Jeong, S., Yesiller, N., Hanson, J.L., Martien, P.T., 2020. Assessment of regional methane emission inventories through airborne quantification in the San Francisco Bay Area. Environ. Sci. Technol. 54, 9254–9264. https://doi.org/10.1021/acs.est.0c01212.

Hamlin, L., Green, R.O., Mouroulis, P., Eastwood, M., Wilson, D., Dudik, M., Paine, C., 2011. Imaging spectrometer science measurements for terrestrial ecology: AVIRIS and new developments. In: 2011 Aerospace Conference. IEEE, pp. 1–7. https://doi.org/10.1109/AERO.2011.5747395.

Hanna, S.R., Briggs, G.A., Hosker Jr., R.P., 1982. Handbook on Atmospheric Diffusion.

Hunter, D., Thorpe, M.J., 2017. Gas Mapping LiDAR Aerial Verification Program Final Report. Alberta Upstream Petroleum Research Fund Project 17-ARPC-03. Petroleum Technology Alliance of Canada (PTAC).

IPCC, 2018. Summary for policymakers. In: Masson-Delmotte, V., Zhai, P., Pörtner, H.-O., Roberts, D., Skea, J., Shukla, P.R., Pirani, A., Moufouma-Okia, W., Péan, C., Pidcock, R., Connors, S., Matthews, J.B.R., Chen, Y., Zhou, X., Gomis, M.I., Lonnoy, E., Maycock, T., Tignor, M., Waterfield, T. (Eds.), Global Warming of 1.5°C. An IPCC Special Report on the Impacts of Global Warming of 1.5°C above Pre-Industrial Levels. Intergovernmental Panel on Climate Change.

Jervis, D., McKeever, J., Durak, B.O.A., Sloan, J.J., Gains, D., Varon, D.J., Ramier, A., Strupler, M., Tarrant, E., 2021. The GHGSat-D imaging spectrometer. Atmos. Meas. Tech. 14, 2127–2140. https://doi.org/10.5194/amt-14-2127-2021.

Johnson, M.R., Conrad, B.M., Tyner, D.R., 2023. Creating Measurement-Based Oil and Gas Sector Methane Inventories using Source-Resolved Aerial Surveys. Submitt. to Commun. Earth Environ. https://doi.org/10.21203/rs.3.rs-2203868/v1 (preprint).

Johnson, M.R., Tyner, D.R., Szekeres, A.J., 2021. Blinded evaluation of airborne methane source detection using Bridger Photonics LiDAR. Remote Sens. Environ. 259, 112418 https://doi.org/10.1016/j.rse.2021.112418.

Kairos Aerospace, 2022. Methane Detection from a Unique Perspective [WWW Document]. URL. https://kairosaerospace.com/methane-detection/ (accessed 5.29.22).

Kass, R.E., Raftery, A.E., 1995. Bayes factors. J. Am. Stat. Assoc. 90, 773–795.

Kemp, C.E., Ravikumar, A.P., 2021. New technologies can cost effectively reduce oil and gas methane emissions, but policies will require careful design to establish mitigation equivalence. Environ. Sci. Technol. 55, 9140–9149. https://doi.org/10.1021/acs.est.1c03071.

Kemp, C.E., Ravikumar, A.P., Brandt, A.R., 2016. Comparing natural gas leakage detection technologies using an open-source "virtual gas field" simulator. Environ. Sci. Technol. 50, 4546–4553. https://doi.org/10.1021/acs.est.5b06068.

Krautwurst, S., Gerilowski, K., Jonsson, H.H., Thompson, D.R., Kolyer, R.W., Iraci, L.T., Thorpe, A.K., Horstjann, M., Eastwood, M., Leifer, I., Vigil, S.A., Krings, T., Borchardt, J., Buchwitz, M., Fladeland, M.M., Burrows, J.P., Bovensmann, H., 2017. Methane emissions from a Californian landfill, determined from airborne remote sensing and in situ measurements. Atmos. Meas. Tech. 10, 3429–3452. https://doi.org/10.5194/amt-10-3429-2017.

Kreitinger, A.T., Thorpe, M.J., 2018. High-Sensitivity Gas-Mapping 3D Imager and Method of Operation, 9970756 B2.

NOAA, 2020. High-Resolution Rapid Refresh (HRRR) Model [WWW Document]. URL. https://rapidrefresh.noaa.gov/ (accessed 6.9.22).

Rashid, K., Speck, A., Osedach, T.P., Perroni, D.V., Pomerantz, A.E., 2020. Optimized inspection of upstream oil and gas methane emissions using airborne LiDAR surveillance. Appl. Energy 275, 115327. https://doi.org/10.1016/j.apenergy.2020.115327.

Ravikumar, A.P., Sreedhara, S., Wang, J., Englander, J.G., Roda-Stuart, D., Bell, C.S., Zimmerle, D.J., Lyon, D.R., Mogstad, I., Ratner, B., Brandt, A.R., 2019. Single-blind inter-comparison of methane detection technologies – results from the Stanford/EDF Mobile Monitoring Challenge. Elem. Sci. Anth 7, 37. https://doi.org/10.1525/elementa.373.

Schwietzke, S., Harrison, M., Lauderdale, T., Branson, K., Conley, S.A., George, F.C., Jordan, D., Jersey, G.R., Zhang, C., Mairs, H.L., Pétron, G., Schnell, R.C., 2019. Aerially guided leak detection and repair: a pilot field study for evaluating the

potential of methane emission detection and cost-effectiveness. J. Air Waste Manage. Assoc. 69, 71–88. https://doi.org/10.1080/10962247.2018.1515123.

Sherwin, E.D., Chen, Y., Ravikumar, A.P., Brandt, A.R., 2021. Single-blind test of airplane-based hyperspectral methane detection via controlled releases. Elem. Sci. Anthr. 9 https://doi.org/10.1525/elementa.2021.00063.

Snipes, M., Taylor, D.C., 2014. Model selection and Akaike information criteria: an example from wine ratings and prices. Wine Econ. Policy 3, 3–9. https://doi.org/10.1016/j.wep.2014.03.001.

Thompson, D.R., Leifer, I., Bovensmann, H., Eastwood, M., Fladeland, M., Frankenberg, C., Gerilowski, K., Green, R.O., Kratwurst, S., Krings, T., Luna, B., Thorpe, A.K., 2015. Real-time remote detection and measurement for airborne imaging spectroscopy: a case study with methane. Atmos. Meas. Tech. 8, 4383–4397. https://doi.org/10.5194/amt-8-4383-2015.

Thorpe, A.K., Frankenberg, C., Aubrey, A.D., Roberts, D.A., Nottrott, A.A., Rahn, T.A., Sauer, J.A., Dubey, M.K., Costigan, K.R., Arata, C., Steffke, A.M., Hills, S., Haselwimmer, C., Charlesworth, D., Funk, C.C., Green, R.O., Lundeen, S.R., Boardman, J.W., Eastwood, M.L., Sarture, C.M., Nolte, S.H., Mccubbin, I.B., Thompson, D.R., McFadden, J.P., 2016. Mapping methane concentrations from a controlled release experiment using the next generation airborne visible/infrared imaging spectrometer (AVIRIS-NG). Remote Sens. Environ. 179, 104–115. https://doi.org/10.1016/j.rse.2016.03.032.

Thorpe, A.K., Frankenberg, C., Thompson, D.R., Duren, R.M., Aubrey, A.D., Bue, B.D., Green, R.O., Gerilowski, K., Krings, T., Borchardt, J., Kort, E.A., Sweeney, C., Conley, S., Roberts, D.A., Dennison, P.E., 2017. Airborne DOAS retrievals of methane, carbon dioxide, and water vapor concentrations at high spatial resolution: application to AVIRIS-NG. Atmos. Meas. Tech. 10, 3833–3850. https://doi.org/10.5194/amt-10-3833-2017.

Thorpe, A.K., Duren, R.M., Conley, S., Prasad, K.R., Bue, B.D., Yadav, V., Foster, K.T., Rafiq, T., Hopkins, F.M., Smith, M.L., Fischer, M.L., Thompson, D.R., Frankenberg, C., McCubbin, I.B., Eastwood, M.L., Green, R.O., Miller, C.E., 2020. Methane emissions from underground gas storage in California. Environ. Res. Lett. 15, 045005 https://doi.org/10.1088/1748-9326/ab751d.

Thorpe, A.K., O'Handley, C., Emmitt, G.D., DeCola, P.L., Hopkins, F.M., Yadav, V., Guha, A., Newman, S., Herner, J.D., Falk, M., Duren, R.M., 2021. Improved methane emission estimates using AVIRIS-NG and an Airborne Doppler Wind Lidar. Remote Sens. Environ. 266, 112681 https://doi.org/10.1016/j.rse.2021.112681.

Tyner, D.R., Johnson, M.R., 2021. Where the methane is—insights from novel airborne LiDAR measurements combined with ground survey data. Environ. Sci. Technol. 55, 9773–9783. https://doi.org/10.1021/acs.est.1c01572.

Varon, D.J., Jacob, D.J., McKeever, J., Jervis, D., Durak, B.O.A., Xia, Y., Huang, Y., 2018. Quantifying methane point sources from fine-scale satellite observations of atmospheric methane plumes. Atmos. Meas. Tech. 11, 5673–5686. https://doi.org/10.5194/amt-11-5673-2018.

Varon, D.J., Jacob, D.J., Jervis, D., McKeever, J., 2020. Quantifying time-averaged methane emissions from individual coal mine vents with GHGSat-D satellite observations. Environ. Sci. Technol. 54, 10246–10253. https://doi.org/10.1021/acs.est.0c01213.